J. Fluid Mech. (2025), *vol.* 1013, A12, doi:10.1017/jfm.2025.10238

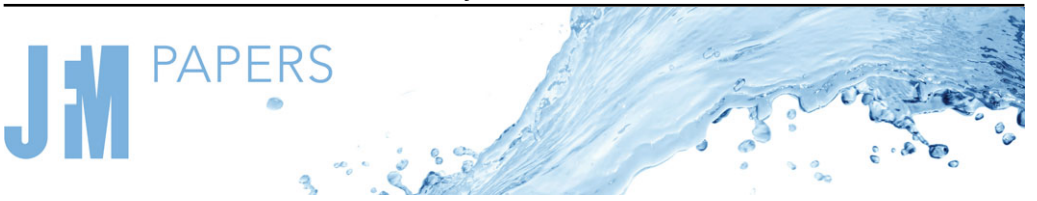

Capsule damage by an enclosed microswimmer

Zhihan Huang[1], **Toshihiro Omori**[1] **and Takuji Ishikawa**[2]

[1]Graduate School of Engineering, Tohoku University, 6-6-01 Aoba, Aoba-ku, Sendai 980-8579, Japan

[2]Graduate School of Biomedical Engineering, Tohoku University, 6-6-01 Aoba, Aoba-ku, Sendai 980-8579, Japan

Corresponding authors: Zhihan Huang, huang.zhihan.p4@dc.tohoku.ac.jp; Toshihiro Omori, omori@tohoku.ac.jp

(Received 23 December 2024; revised 26 March 2025; accepted 6 May 2025)

Capsules are widely used in bioengineering, chemical engineering and industry. The development of drug delivery systems using deformable capsules is progressing, yet the regulation of drug release within a capsule remains a challenge. Meanwhile, a microswimmer enclosed in a capsule can generate a large lubrication force on the capsule membrane, which could result in deformation and mechanical damage to the membrane. In this study, we numerically investigate how a capsule can be damaged by an enclosed microswimmer. The capsule membrane is modelled as a two-dimensional neo-Hookean material, with its deformability parametrised by capillary number. An isotropic brittle damage model is applied to express membrane rupture, with the Lighthill–Blake squirmer serving as the microswimmer model. In a sufficiently small capillary number regime, pusher-type squirmers exhibit stable swimming along the capsule membrane, while neutral-type and puller-type squirmers exhibit swimming towards the membrane and remain stationary. As capillary number increases, the damage to the membrane increases and rupture occurs in all swimming modes. For pusher-type squirmers, the critical capillary number leading to rupture is dependent on the initial incidence angle, whereas neutral-type and puller-type squirmers are independent of the initial value. Furthermore, we present methods for controlling membrane damage by magnetically orienting the microswimmer. The findings reveal that a static magnetic field can orient the microswimmer, leading to membrane damage and rupture even for a capsule that cannot be damaged by free swimming, while controlling the swimming path with a rotating magnetic field enables soft membranes to maintain deformation without rupture.

Key words: capsule/cell dynamics, membranes, active matter

1. Introduction

Capsules are droplets enclosed by a thin elastic membrane and are found in various situations, such as red blood cells and fish eggs in nature, cosmetics and agricultural products in industrial processes. They are therefore widely used in fields such as bioengineering and chemical engineering. In the agricultural field, Friedman & Mualem (1994) conducted a study on the diffusion of fertilisers into soil from capsules. They investigated the influence of membrane conductance and capsule density on the fertiliser release rate, and managed to achieve the desired release rate using their proposed model. In the field of biomedical engineering, encapsulation techniques have been used for targeted drug delivery (Shi & Tan 2002; Skirtach *et al.* 2008; Bhujbal, de Vos & Niclou 2014; Kamat *et al.* 2024), and controlled release of the drug in capsules has become an important issue. To consider this issue, controlled release of certain substances has been achieved by varying the permeability of the capsule membrane. For example, Kamat *et al.* (2024) changed the ratio of complexing chitosan and calcium-alginate in the capsule membrane, and controlled the release rate of NaFeCN within the mortar. Skirtach *et al.* (2008) made aggregates of gold nanoparticles in polyelectrolyte shells, and changed the capsule permeability by near-infrared illumination. Bhujbal *et al.* (2014) used liposomes to contain active cytotoxic compounds, and managed to release those compounds in the long term to treat brain tumours. They changed the ratio of phospholipid and cholesterol in liposomes to obtain different release rates. Shi & Tan (2002) conducted research on encapsulating vitamin D_2 within a capsule made of chitosan. They found that the capsule can achieve sustained release in the intestine juice and delayed release in the gastric environment by changing the molecular weight and concentration of chitosan. Despite the advent of sophisticated control techniques for membrane permeability by employing light irradiation and chemical concentration fields, viscous forces also play an important role in membrane mechanics. The viscous stress exerted on the capsule membrane by the surrounding fluid flow has the potential to cause damage to the membrane and result in the unintended release of drugs. Consequently, it is imperative to undertake a comprehensive study of the motion and deformation of capsules within the context of fluid flow.

Theories of capsule dynamics have been developed sufficiently by Barthès-Biesel, Pozrikidis and their colleagues. As outlined in the seminal work of Pozrikidis (2010), an overview of capsule dynamics can be found in the Introduction. Barthès-Biesel (1980) conducted an analytical study on the dynamics of a microcapsule under linear shear flow, deriving an analytical solution in the limit of small deformation. In order to extend this to large deformations, Barthès-Biesel *et al.* (2002) investigated the mechanical properties of two-dimensional hyperelastic materials with different constitutive laws. Lac *et al.* (2004) then undertook a numerical investigation into a spherical capsule in three-dimensional Stokes flow. The numerical results obtained by the researchers were in agreement with the prediction made by Barthès-Biesel *et al.* (2002), although the computation became unstable in the case of large deformation. As demonstrated by Walter *et al.* (2010), the development of a coupled finite element and boundary element method has enabled the stabilisation of computations. This methodology has been employed successfully to quantify the transition capillary numbers of different deformation regimes for various constitutive laws.

Foessel *et al.* (2011) have also investigated the influence of the viscosity ratio of internal to external fluids. Their findings indicate that the internal viscosity exerts a significant effect on capsule deformation when the internal viscosity is smaller than that of the external environment. Conversely, when the internal viscosity exceeds that of the external environment, the internal motion's decelerating effect on the capsule deformation is diminished. Omori *et al.* (2012) conducted a numerical study of a non-spherical capsule

in creeping shear flow, the results of which demonstrate that the orientation of a non-spherical capsule is subject to variation under time reversal, and that this variation can be controlled by adjusting the background flow strength or unsteadiness. Dupont *et al.* (2015) conducted an investigation into the influence of the bending resistance of a spherical capsule. The findings of the study indicate that the wrinkle wavenumber of the membrane is contingent solely on the bending resistance, and that the bending resistance exerts an influence on local buckling. However, its effect on shape and deformation can be disregarded. Matsunaga *et al.* (2015) investigated capsule deformation under oscillating shear flow, finding that deformation is larger under oscillation than under steady shear flow, and that the overshoot is also larger when the capsule is softer. Matsunaga *et al.* (2016) also conducted a numerical investigation of the capsule dynamics in their dense suspensions. It was observed that as the volume fraction of the capsules increased, the capsule deformation increased correspondingly; however, the angle of inclination of the capsules with respect to the flow direction decreased.

However, as the deformation increases, the capsule will inevitably sustain damage due to the substantial deformation that it undergoes. Consequently, research into membrane damage due to mechanical stress has been undertaken both experimentally and theoretically (Chang & Olbricht 1993; Walter, Rehage & Leonhard 2001; Husmann *et al.* 2005; Koleva & Rehage 2012; Leopércio *et al.* 2021; Jambon-Puillet, Jones & Brun 2020). As demonstrated by Chang & Olbricht (1993), the insertion of a capsule into Couette flow resulted in the observation of capsule deformation. Furthermore, capsule break-up was observed when the deformation induced by the flow reached a sufficient magnitude. Walter *et al.* (2001) conducted experiments on a capsule within shear flow, observing shape oscillation and membrane folding phenomena, which have the potential to lead to fatigue mechanisms. Leopércio *et al.* (2021) conducted a microfluidic experiment in which they observed the flow of microcapsules through constricted channels. The rupture of microcapsules was found to be initiated by stress caused by deformation, which in turn is influenced by capsule diameter and thickness. Jambon-Puillet *et al.* (2020) conducted experiments on the impact of capsules against rigid walls. The impact velocity of the capsules was found to have a significant effect on their deformation and rupture. Furthermore, the viscosity of the surrounding fluid was found to influence the critical velocity at which rupture occurs.

Moreover, Husmann *et al.* (2005) exposed a microcapsule to centrifugal forces, and observed its destruction as a result of the substantial centrifugal force applied. The rupture of the capsule was found to occur exclusively at the pole ends. As stated by Koleva & Rehage (2012), the wrinkling and break-up of microcapsules in extreme large deformation was observed through the introduction of microcapsules into shear flow. Furthermore, Grandmaison, Brancherie & Salsac (2021) presented a numerical model of capsule damage and rupture, considering damage behaviour within the framework of continuum damage mechanics. The damage model employed was of the isotropic brittle damage type, with the membrane damage state being dependent on the history of loading.

The flow applied to a capsule is not limited to background flows; it could also be the flow created by external forces or microswimmers of the same size as the capsule. In their study, Kree, Rückert & Zippelius (2021) examined the impact of diverse external forces on the locomotion of a droplet, encompassing a single point force, a force dipole, and even the forces generated by a biflagellate swimmer. In the context of microswimmers, the squimer model developed by Lighthill (1952) has been seminal. This model, the basis of the present study, propels itself by generating small deformations on the particle surface. It was later expanded upon by Blake (1971) to create a more generalised microswimmer model, corresponding to a microswimmer that propels itself by generating slip velocities

on its surface (Ishikawa 2024*a*). This is the best-known self-propelled particle model in microfluid dynamics. As demonstrated in the works of Reigh *et al.* (2017) and Huang, Omori & Ishikawa (2020), the interaction between squirmers and droplets has been the subject of numerous studies. In particular, Reigh *et al.* (2017) conducted a numerical simulation of a squirmer enclosed within a droplet, thereby demonstrating that the enclosed squirmer is capable of propelling the droplet through hydrodynamic interactions. Furthermore, the co-swimming state exhibited by both the squirmer and the droplet was found to be stable. As stated by Huang *et al.* (2020), a self-propelled droplet model analogous to a squirmer has also been documented. This model demonstrates that the collective swimming of squirmers within a drop engenders a flow on the drop's surface, which subsequently swims due to its slip velocity. The aforementioned models operated under the assumption that the surface tension of the droplet is considerably larger than the viscous stress of the flow. Consequently, the deformation or breakdown of the droplet was not taken into consideration. In considering the deformation of droplets due to a microswimmer's swimming, Kawakami & Vlahovska (2025) conducted an analytical study of an active particle confined within a spherical, deformable droplet. It was established that an active particle offset from the centre of the drop can disrupt the symmetry, resulting in shape changes and droplet displacement.

Additionally, there has been considerable research activity on the deformation of capsules and vesicles due to the movement of microswimmers (Dias & Powers 2013; Daddi-Moussa-Ider *et al.* 2019; Takatori & Sahu 2020; Vutukuri *et al.* 2020; Nagard *et al.* 2022; Fessler *et al.* 2024; Wu, Omori & Ishikawa 2024). Dias & Powers (2013) conducted a study on the locomotion of an infinitely long swimmer in proximity to a deformable boundary that separates the fluid into two distinct parts. The direction of fluid flow can be controlled by manipulating the viscosity ratio on either side of the swimmer. Subsequently, when microswimmers are located outside of capsules and vesicles, Daddi-Moussa-Ider *et al.* (2019) developed a simple model to describe the interaction of a self-driven spherical particle with a minimal membrane system, allowing for both penetration and trapping. It has been demonstrated that the active particle may either become trapped in proximity to the membrane or penetrate through it. In the latter case, the membrane may be permanently destroyed or recover its initial shape by means of self-healing. Concurrently, Fessler *et al.* (2024) investigated the interaction of Janus colloids with giant vesicles, leading to the observation of endocytosis. The study indicated the pivotal function of far-field hydrodynamic interaction, determining that puller-type swimmers possess the capacity to target giant vesicles, deform their membranes, and achieve stable engulfment. In addition, a numerical simulation of a squirmer swimming in a suspension of red blood cells was conducted by Wu *et al.* (2024), which revealed that a squirmer can swim faster than a passive swimmer by repelling red blood cells to the side of the squirmer. Furthermore, the influence of microswimmers inside capsules and vesicles is also investigated. In their research, Vutukuri *et al.* (2020) conducted numerical simulations, placing self-propelled particles within giant unilamellar vesicles, and observing the resultant non-equilibrium shapes and active membrane fluctuations induced by the particles. Similarly, Takatori & Sahu (2020) conducted experiments but replaced the particles with bacteria and derived an analytical solution. Subsequently, Nagard *et al.* (2022) encapsulated bacteria within giant lipid vesicles, thereby forming a tube-like structure that can transform into an effective helical flagellum and propel the vesicle. The development of a theoretical model to estimate the propulsive force and efficiency is also reported.

Furthermore, external magnetic fields and lasers have been utilised to regulate the movement of the swimmers. For instance, as cited in Huang *et al.* (2016), the incorporation of magnetic particles into a near-infrared responsive material has enabled the fabrication

of a self-folding microrobot that is powered by magnetism. Lozano *et al.* (2016) conducted experiments by subjecting a spherical active colloid exposed to an inhomogeneous laser field. The outcomes of these studies demonstrate that the transportation of active colloids can be directed towards lower laser intensity, and that the motion of active colloids can be modulated by adjusting the laser field.

Notwithstanding the exhaustive research that has been carried out in this field, the precise mechanisms by which microswimmers are confined within elastic capsules, and the effects of the flow generated by them on the capsule membrane, remain to be elucidated. The present study focuses on the hydrodynamic interaction between the capsule membrane and the microswimmer. This is done with a view to determining the effect on capsule membrane damage and rupture. Moreover, the objective of the present study is to develop a damage control technique that utilises an external magnetic torque. In § 2, we present our numerical models of a capsule, the damage behaviour of the capsule membrane and a microswimmer, together with the fundamental equations and our numerical method. In § 3, we present the simulation results obtained under various conditions, and provide a range of different capsule states. In § 4, an external magnetic field is imposed in order to control the squirmer orientation and to investigate damage control techniques using the external magnetic torque. The conclusions of this study are outlined in § 5.

2. Governing equations and numerical method

Consider a capsule immersed in an unbounded incompressible Newtonian liquid with viscosity μ and density ρ. The capsule contains the same liquid as the exterior and a spherical microswimmer with radius a_s, as shown in figure 1(*a*). The reference shape of the capsule is assumed to be a sphere with radius a_c. Due to the small size of both capsule and microswimmer, the Reynolds number is small enough that the flow field can be considered as Stokes flow, where inertia can be neglected. The thickness of the capsule membrane is sufficiently small compared to its size and curvature radius, thus the membrane is considered as a two-dimensional hyperelastic material. To estimate the damage to the capsule due to hydrodynamic interaction with the microswimmer, we employ a continuum-based isotropic brittle damage model, as described previously by Grandmaison *et al.* (2021).

The ensuing sections are to be perused with a view to acquiring an understanding of the governing equations of fluid–solid interactions between the capsule and the microswimmer.

2.1. *Membrane mechanics*

Assume that the membrane thickness is sufficiently small for the membrane to be considered as a two-dimensional hyperelastic material. The membrane surface S is determined by two surface curvilinear coordinates (ξ^1, ξ^2). The membrane material points in the reference and deformed states are given by $\boldsymbol{X}(\xi^1, \xi^2)$ and $\boldsymbol{x}(\boldsymbol{X}, t)$, respectively. The gradient of transformation, denoted by $\boldsymbol{F}$, is given by (Pozrikidis 2010)

$$\mathrm{d}\boldsymbol{x} = \boldsymbol{F} \cdot \mathrm{d}\boldsymbol{X}. \tag{2.1}$$

Then the local deformation of the membrane can be measured by the Green–Lagrange strain tensor

$$\boldsymbol{E} = \tfrac{1}{2}\left(\boldsymbol{F}^T \cdot \boldsymbol{F} - \boldsymbol{I}\right), \tag{2.2}$$

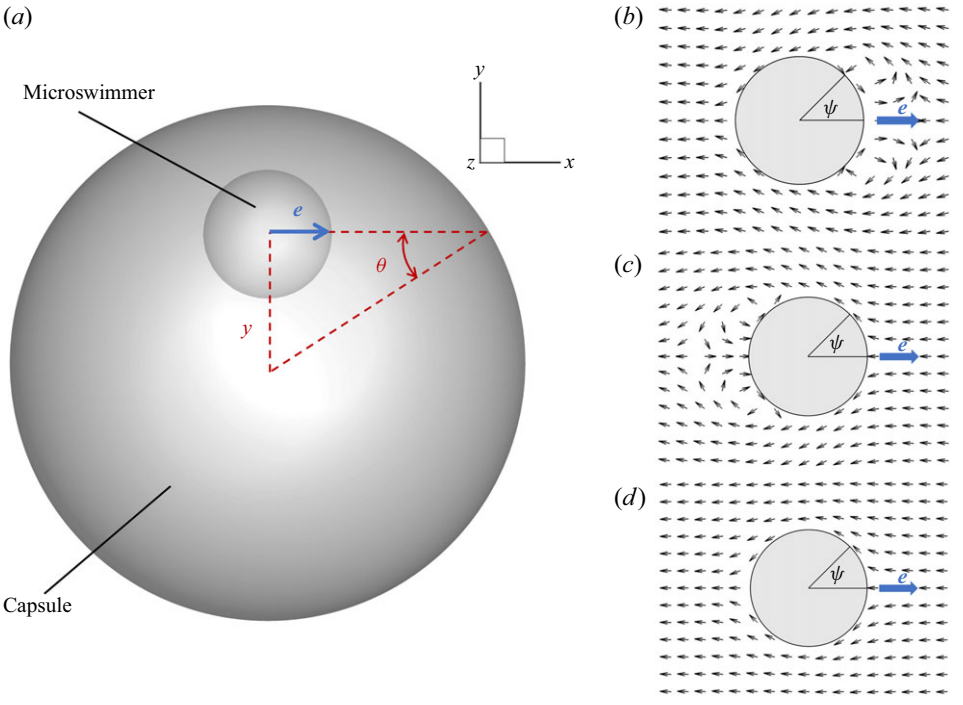

Figure 1. Problem setting of the numerical simulation. (*a*) A spherical capsule of radius a_c is immersed in an infinite Newtonian liquid of density ρ and viscosity μ (the centre of mass of the capsule corresponds to the Cartesian origin). The inner liquid of the capsule is assumed to be the same as the external liquid. A squirmer of radius a_s is contained within the capsule, and the size ratio is fixed to $a_c/a_s = 4$. The squirmer orientation $\boldsymbol{e}$ is initially set to (1, 0, 0), and the initial centre of the squirmer is (0, y, 0) . The initial incidence angle θ is determined by adjusting the initial position y. (*b–d*) The flow created by the squirmer with different swimming modes: (*b*) a pusher-type squirmer ($\beta = -3$); (*c*) a puller-type squirmer ($\beta = 3$); and (*d*) a neutral-type squirmer ($\beta = 0$).

where $\boldsymbol{I}$ is the identity tensor. And two invariants of the transformation are given by

$$I_1 = \lambda_1^2 + \lambda_2^2 - 2, \quad I_2 = \lambda_1^2\lambda_2^2 - 1 = J_s^2 - 1, \tag{2.3}$$

where λ_1, λ_2 are the principal dilation ratios, and the Jacobian $J_s = \lambda_1\lambda_2$ expresses the ratio of the deformed to the undeformed surface areas. Assuming that the membrane is an isotropic material, Cauchy tension tensor $\boldsymbol{T}$ can be related to a strain energy function per unit area of undeformed membrane $\omega_s(I_1, I_2)$ by the equation

$$\boldsymbol{T} = \frac{1}{J_s}\boldsymbol{F}\cdot\frac{\partial\omega_s}{\partial\boldsymbol{E}}\cdot\boldsymbol{F}^T. \tag{2.4}$$

The behaviour of the capsule membrane is described by means of a neo-Hookean (NH) law, the strain energy function of which is given by

$$\omega_s^{NH} = \frac{G_s}{2}\left(I_1 - 1 + \frac{1}{I_2 + 1}\right), \tag{2.5}$$

where G_s is the surface elastic shear modulus.

In the case of an infinitely thin membrane, the inertia of the membrane can be considered negligible. Consequently, the motion of the membrane is governed by local mechanical equilibrium:

$$\boldsymbol{q}_e + \nabla_s \cdot \boldsymbol{T} = \boldsymbol{0}, \tag{2.6}$$

where $\boldsymbol{q}_e$ is the surface load due to membrane in-plane stretch, and ∇_s is the surface divergence operator. By applying the virtual work principle, the equilibrium equation (2.6) can be written in a weak form (Walter *et al.* 2010)

$$\iint_s \hat{\boldsymbol{v}} \cdot \boldsymbol{q}_e \, \mathrm{d}S - \iint_s \hat{\boldsymbol{\epsilon}}(\hat{\boldsymbol{v}}) : \boldsymbol{T} \mathrm{d}S = 0, \tag{2.7}$$

where $\hat{\boldsymbol{v}}$ and $\hat{\boldsymbol{\epsilon}}(\hat{\boldsymbol{v}}) = (1/2)(\nabla_s \hat{\boldsymbol{v}} + \nabla_s \hat{\boldsymbol{v}}^T)$ are the virtual displacement and virtual deformation tensor, respectively.

The equilibrium equation under consideration pertains to in-plane deformation and does not encompass the bending stiffness of the membrane. This renders the calculations highly unstable for compressive deformations, thus necessitating the use of a weak bending energy in this study. It is assumed that the in-plane deformation load and the bending deformation load can be expressed as a linear sum due to the sufficiently small membrane thickness, and Helfrich's model (Helfrich 1973) is adopted for the bending energy:

$$\omega_b = \frac{E_b}{2} \int (2H - c_0) \, \mathrm{d}S, \tag{2.8}$$

where E_b is the bending modulus, H is the mean curvature of the surface, and c_0 is spontaneous curvature. Assume that the reference curvature is a flat shape, i.e. $c_0 = 0$, and the bending force density $\boldsymbol{q}_b$ is expressed by the first variant of the bending energy (Ou-Yang & Helfrich 1989):

$$\boldsymbol{q}_b = -2E_b[\Delta_s H + 2H(H^2 - K)]\boldsymbol{n}, \tag{2.9}$$

where Δ_s is the Laplace–Beltrami operator on the surface, K is the Gaussian curvature, and $\boldsymbol{n}$ is the normal vector on the surface to the outside. Thus the membrane load due to the elastic deformation $\boldsymbol{q}_c$ is determined by $\boldsymbol{q}_c = \boldsymbol{q}_e + \boldsymbol{q}_b$. The findings of Dupont *et al.* (2015) demonstrate that the effect of bending resistance is negligible in comparison to the effect of in-plane stretch. Consequently, the influence of bending resistance on the shape and deformation can be disregarded.

2.2. *Damage behaviour*

The model proposed by Grandmaison *et al.* (2021) is employed to delineate the damage to a two-dimensional membrane. The damage is modelled on the basis of continuum damage mechanics, with the damage state being defined as an isotropic brittle damage model, and the damage state determined by the history of loading.

We assume that the transformations of the capsule wall correspond to isothermal elastic deformation and damage. The damage variable represents the irreversible growth of microdefects in infinitesimal elements. Here, an overview of the work of Grandmaison *et al.* (2021) will be provided, with the aim of elucidating the brittle damage model.

Assume the presence of irreversible microdefects growing within the membrane in response to large deformations. The deformation is assumed to be isothermal elastic deformation, and the damage is defined by the irreversible growth of microdefects in the infinitesimal element. It is also assumed that the growth of the microdefects in the element is isotropic. Thus the microdefects have no preferential orientation, and the damage variable can be expressed by a scalar function d, which is defined as $d = \delta S_D/\delta S = 1 - \delta\tilde{S}/\delta S$, where δS is the total area of the infinitesimal element including the microdefects, and δS_D is the maximum intersection of microdefects in δS. The function d

ranges from 0, for the local undamaged state, to 1, indicating the crack having the size of the element.

By using the principle of strain equivalence (Grandmaison *et al.* 2021), tension in the damaged state can be written as

$$\tilde{\boldsymbol{T}} = \frac{\delta \tilde{S}}{\delta S}\boldsymbol{T} = (1-d)\boldsymbol{T}, \tag{2.10}$$

where $\boldsymbol{T}$ is calculated from an undamaged material. According to classical continuum damage mechanics, strain energy in the damaged state is assumed to be homogeneous, and the strain energy function of a damaged neo-Hookean membrane can be written as

$$\omega_s(I_1, I_2, d) = (1-d)\omega_s^{NH}(I_1, I_2). \tag{2.11}$$

By introducing the damage threshold function (Besson *et al.* 2010) and model for quasi-brittle damage developed by (Marigo 1985), the damage variable d can be calculated by

$$d = \langle \zeta(\omega_s^{NH^{MAX}}) \rangle^+, \tag{2.12}$$

where $\langle\,\rangle^+$ is the Macaulay bracket defined by

$$\langle x \rangle^+ = \begin{cases} x & \text{if } x \geqslant 0, \\ 0 & \text{otherwise}, \end{cases} \tag{2.13}$$

and $\zeta(\omega_s^{NH^{MAX}})$ is given by

$$\left.\begin{aligned} \zeta\left(\omega_s^{NH^{MAX}}\right) &= \left(\omega_s^{NH^{MAX}} - Y_D\right)/Y_C, \\ \omega_s^{NH^{MAX}}(t) &= \max_{\tau \leqslant t}\ \omega_s^{NH}(t), \end{aligned}\right\} \tag{2.14}$$

where t indicates the time, and $Y_D \geqslant 0$ and $Y_C > 0$ represent damage threshold and hardening modulus, respectively.

Grandmaison *et al.* (2021) showed the sheer increase of the damage variable d before rupture, and it is classical in damage mechanics to relax the criterion for rupture to $d = 0.9$ or even $d = 0.8$. In this paper, we consider $d = 0.9$ as the criterion for membrane rupture.

In this context, a material is said to be in a damaged state if the strain energy ω_s attains a value greater than the damage threshold Y_D. Conversely, if the strain energy remains below the damage threshold at all times, then the material is designated as undamaged. The categorisation of the damage state is dependent on the final value of d in the results of the simulation. The damage state is divided into three distinct regimes, namely (i) the undamaged state ($d = 0$), (ii) the damaged state ($0 < d < 0.9$), and (iii) the rupture state ($d \geqslant 0.9$). In addition, given that the damage variable d corresponds to the irreversible growth of microdefects in the capsule, it can be concluded that the value of d will be permanently recorded even when deformation of the capsule ceases.

2.3. *Swimmer model*

The microswimmer is modelled after the Lighthill–Blake squirmer (Lighthill 1952; Blake 1971), a model of a self-propelling sphere by its surface velocity $\boldsymbol{u}^s$. The squirmer with the unit orientation vector $\boldsymbol{e}$ exhibits axisymmetric and steady surface squirming velocities. The flow field surrounding the squirmer has been derived as an infinite series of eigensolutions of the Stokes equation in axisymmetric spherical polar coordinates (r, ψ). The origin of the coordinate system is located at the centre of the squirmer, with r denoting the radial position, and ψ the angle from the unit orientation vector $\boldsymbol{e}$, as illustrated

in figure 1. We follow Ishikawa, Simmonds & Pedley (2006) and consider the tangential velocities up to the second mode. The surface velocity is then given by

$$u_r(r,\psi)=0, \quad u_\psi(r,\psi)=B_1\sin\psi+B_2\sin\psi\cos\psi, \tag{2.15}$$

where swimming speed U_0 is then given by $U_0=(2B_1)/3$. The swimming mode and the stresslet strength of the squirmer are controlled by the squirmer parameter $\beta=B_2/B_1$: $\beta<0$ corresponds to a pusher-type squirmer that has a propulsion apparatus behind the body; $\beta>0$ corresponds to a puller-type squirmer that has a propulsion apparatus in front of the body; $\beta=0$ corresponds to a neutral-type squirmer that has a propulsion apparatus at the centre of the body (see figure 1*b*,*c*,*d*).

2.4. *Flow due to the capsule deformation and the squirmer*

In the context of viscous-dominant fluid flow, the flow field is governed by the Stokes equation. The flow field is thus described by a boundary integral equation with the Green's function. The flow resulting from the deformation of the capsule and the squirmer can be derived as

$$\boldsymbol{u}(\boldsymbol{x})=-\frac{1}{8\pi\mu}\left[\int_{S_c}\boldsymbol{J}(\boldsymbol{x},\boldsymbol{y})\cdot\boldsymbol{q}_c(\boldsymbol{y})\,\mathrm{d}S_c(\boldsymbol{y})+\int_{S_s}\boldsymbol{J}(\boldsymbol{x},\boldsymbol{y})\cdot\boldsymbol{q}_s(\boldsymbol{y})\,\mathrm{d}S_s(\boldsymbol{y})\right], \tag{2.16}$$

where $\boldsymbol{q}_s$ is the viscous load exerted on the squirmer, and the subscripts c and s represent the capsule and squirmer surfaces, respectively. The Green's function of the Stokeslet $\boldsymbol{J}$ is defined by

$$\boldsymbol{J}(\boldsymbol{x},\boldsymbol{y})=\frac{\boldsymbol{I}}{r}+\frac{1}{r^3}\boldsymbol{r}\otimes\boldsymbol{r}, \tag{2.17}$$

where $\boldsymbol{r}=\boldsymbol{x}-\boldsymbol{y}$, $r=|r|$ and $\boldsymbol{I}$ is the identity tensor.

The determination of the viscous load on the capsule membrane, designated as $\boldsymbol{q}_c$, can be achieved through the application of membrane mechanics, as elucidated in §§ 2.1 and 2.2, while the load on the squirmer, denoted as $\boldsymbol{q}_s$, is unknown. From the boundary condition of the rigid motion of squirmer, the following equation holds: $\boldsymbol{u}=\boldsymbol{U}+\boldsymbol{\Omega}\times\hat{\boldsymbol{r}}+\boldsymbol{u}^s$ when $\boldsymbol{x}\in S_s$, where $\boldsymbol{U}$ is the translational velocity, $\boldsymbol{\Omega}$ is the angular velocity, $\hat{\boldsymbol{r}}=\boldsymbol{x}-\boldsymbol{x}_g$, and $\boldsymbol{x}_g$ is the centre of the squirmer. In addition, the force-free and torque-free conditions are given by

$$\int\boldsymbol{q}_s\,\mathrm{d}S_s=\boldsymbol{0} \tag{2.18}$$

and

$$\int\boldsymbol{q}_s\times\hat{\boldsymbol{r}}\,\mathrm{d}S_s=\boldsymbol{0}. \tag{2.19}$$

We solve for the three unknowns $\boldsymbol{q}_s$, $\boldsymbol{U}$ and $\boldsymbol{\Omega}$ by coupling (2.16), (2.18) and (2.19). Detailed numerical methods are explained in the next subsection.

2.5. *Numerical method*

In order to compute the fluid–solid interactions, the finite element–boundary element coupling method is employed for the capsule deformation (Walter *et al.* 2010), and a series of linear equations is discretised by the boundary element method for the squirmer motion (Huang *et al.* 2020). The capsule membrane is discretised into 20 480 triangular elements with 10 242 nodes, while the squirmer surface is discretised into 1280 triangular elements with 642 nodes.

All material points are tracked in a Lagrangian manner, and the strain energy and Cauchy tension can be calculated explicitly at any time. The equilibrium equation (2.7) is solved with respect to $\boldsymbol{q}_e$ by a finite element method (Walter *et al.* 2010). The bending force density $\boldsymbol{q}_b$ is determined from the local mean and Gaussian curvatures according to (2.9), and the load $\boldsymbol{q}_c$ on the capsule membrane is calculated by summing $\boldsymbol{q}_e$ and $\boldsymbol{q}_b$. Substituting $\boldsymbol{q}_c$ into (2.16), the flow generated by the capsule deformation, i.e. the first term of the equation, is computed by a Gaussian numerical integration scheme (Huang *et al.* 2020). To find the surface load on the squirmer $\boldsymbol{q}_s$, the following simultaneous linear equations are formulated from the boundary integral equation at $\boldsymbol{x} \in S_s$ and the force and torque balance (Huang *et al.* 2020):

$$\begin{bmatrix} \mathcal{J} & \mathcal{M}_1 & \mathcal{M}_2 \\ \mathcal{F} & \mathbf{0} & \mathbf{0} \\ \mathcal{T} & \mathbf{0} & \mathbf{0} \end{bmatrix} \begin{bmatrix} \boldsymbol{q}_s \\ \boldsymbol{U} \\ \boldsymbol{\Omega} \end{bmatrix} = \begin{bmatrix} -\boldsymbol{u}^c + \boldsymbol{u}^s \\ \mathbf{0} \\ \mathbf{0} \end{bmatrix}, \tag{2.20}$$

where the matrix component $\mathcal{J}$ is computed by the second term of (2.16), $\mathcal{F}$ and $\mathcal{T}$ are given by (2.18) and (2.19), $\mathcal{M}_1$ and $\mathcal{M}_2$ are the mobility matrices given by the boundary condition, and the velocity $\boldsymbol{u}^c$ is the flow generated by the capsule deformation. The total matrix size is $(3N+6) \times (3N+6)$, and the dense matrix system is solved by a lower and upper factorisation technique (Huang *et al.* 2020), where $N = 642$ is the number of computational points. After solving (2.20), the translational $\boldsymbol{U}$ and rotational $\boldsymbol{\Omega}$ velocities of the squirmer are obtained, and each nodal point on the squirmer surface is updated by the second-order Runge–Kutta method. The flow field is also updated by substituting $\boldsymbol{q}_s$ into (2.16), and new positions of the capsule membrane are given in the same way with the no-slip boundary condition $\mathrm{d}\boldsymbol{x}/\mathrm{d}t = \boldsymbol{u}$.

When the squirmer comes too close to the capsule surface, the solution becomes less accurate and numerical instabilities may arise. To avoid this, we add short-range repulsive forces between the capsule and the squirmer, i.e. providing a force dipole against the nearest neighbour surface of the capsule and the squirmer.

The repulsive force is given by the following equation as an exponentially decaying function, as in previous studies (Brady & Bossis 1985; Ishikawa *et al.* 2006):

$$\boldsymbol{F}_{rep} = \alpha_1 \frac{\alpha_2 \exp(-\alpha_2 r)}{1 - \exp(-\alpha_2 r)}(-\boldsymbol{r}), \tag{2.21}$$

where $\boldsymbol{r}$ is the vector connecting two nodes, $r = |\boldsymbol{r}|$, and α_1, α_2 are the magnitude of the repulsive force and a parameter related to distance between two nodes. The stress acting on node i is computed by $\boldsymbol{F}^i_{rep}/A_i$, where A_i is the area of the Voronoi cell of node i.

In this study, we choose $\alpha_1 = 1000$ and $\alpha_2 = 50$, corresponding to an effective working distance of the repulsive force of the order of $r/a_s = 0.2$. This value is nearly equal to the mesh size $\Delta x/a_s \sim 0.1$ and can be seen to work only when the swimmer and the capsule are sufficiently close together. When a repulsive force is acting, the force balance of (2.18) changes as follows:

$$\int \boldsymbol{q}_s \, \mathrm{d}S_s = \boldsymbol{F}_{rep}. \tag{2.22}$$

Another parameter, the capillary number, is defined as $Ca = \mu U_0/G_s$, expressing the ratio of viscous force and elastic force. In our simulations, all equations are non-dimensionalised by the free-swimming velocity U_0, the radius of microswimmer a_s, the viscosity μ, and the elastic modulus G_s. The dimensionless bending rigidity is set to $E_b/G_s a_s^2 = 0.01$, and the size ratio between capsule and squirmer is $a_c/a_s = 4.0$

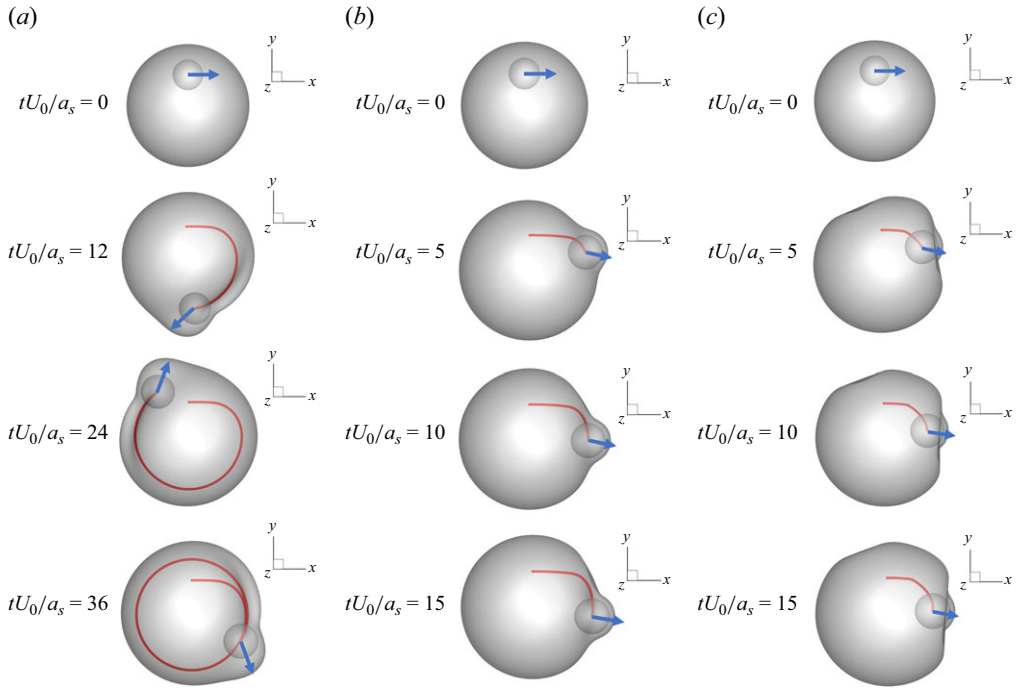

Figure 2. Swimming trajectory of a squirmer with different swimming modes in the undamaged regime; each snapshot indicates the time sequence. The incidence angle is set to $\theta = 30°$ for all cases. (*a*) A pusher-type squirmer ($\beta = -3$) case with $Ca = 0.1$. (*b*) A neutral-type squirmer ($\beta = 0$) case with $Ca = 0.07$. (*c*) A puller-type squirmer ($\beta = 3$) case with $Ca = 0.09$. A pusher-type squirmer circles stably near the capsule membrane, while a neutral-type or puller-type squirmer swims perpendicularly towards the membrane, reaching equilibrium at $tU_0/a_s \geqslant 15$. Blue arrows corresponds to the orientation vector $\boldsymbol{e}$.

throughout the study. As for damage behaviour of the capsule, we set $Y_D/G_s = 0.2$, $Y_C/G_s = 2.0$. A dimensionless time step $\Delta t\ U_0/a_s$ is set to $\Delta t\ U_0/a_s = 5.0 \times 10^{-4}$.

3. Damage to the membrane caused by an internal squirmer

3.1. *Elastic deformation without damage to membranes*

First, the capsule deformation is considered in the low capillary number regime. The swimming mode of the squirmer is set to $\beta = -3$, corresponding to a pusher-type squirmer. The orientation of the squirmer is set to $\boldsymbol{e} = (1, 0, 0)$, and the initial swimming direction is aligned with its orientation. The initial position of the squirmer is set to $(x/a_s, y/a_s, z/a_s) = (0, 2, 0)$, which corresponds to the initial incidence angle $\theta = 30°$ as shown in figure 1(*a*). The mass centre of the capsule is initially placed at (0, 0, 0), and the capillary number is set as $Ca = 0.1$.

As illustrated in figure 2(*a*), the temporal development of the swimmer's trajectory is demonstrated.

Subsequent to the initiation of the calculation, the swimming direction of the squirmer is modified by hydrodynamic interactions with the membrane, resulting in the adoption of a circular trajectory along the capsule membrane. In the low Ca regime, the strain energy does not reach the threshold for brittle damage due to the small deformation of the membrane. Consequently, deformation of the membrane invariably occurs within the elastic region, without compromising the integrity of the membrane.

The same tendency can be observed for the puller-type and neutral-type squirmers, but their swimming trajectories are different from those of the pusher-type squirmer (cf. figure 2*b*,*c*). In the cases of neutral-type and puller-type squirmers ($\beta = 0, 3$), the squirmer swims towards the membrane and finally comes to rest in a position of equilibrium.

As demonstrated in figure 2(*c*), a dimple is also visible at the upper part of the capsule. The observed asymmetric distribution can be attributed to the initial conditions. Specifically, the initial position of the swimmer is near the top of the capsule, and the dimple manifests at the top of the capsule. Conversely, if the swimmer is initially positioned at the bottom, then the dimple will also appear at the bottom.

The underlying reason for these trajectory differences is elucidated in Ishikawa (2019) by lubrication theory, where a pusher-type squirmer tends to escape from a free surface, while a puller-type squirmer tends to be trapped by a free surface. It is important to note that the findings of the present study demonstrate discrepancies with those of previous research. For instance, while the literature suggests that a neutral-type squirmer will typically escape from a free surface, our study demonstrates that it swims towards the capsule membrane. This deviation can be attributed to the deformation of the capsule membrane, which, upon being deformed around the squirmer, cancels out the rotational torque generated on the opposite side. Consequently, the torque generated in front of the squirmer is insufficient to alter its direction, resulting in the neutral-type squirmer swimming towards the capsule surface.

3.2. *Effect of capillary number; three different states of membrane damage*

The subsequent investigation focuses on the effect of capillary number. A pusher-type squirmer ($\beta = -3$) is confined within the capsule, and the initial conditions are the same as in figure 2; we observed three distinct states of membrane damage, which varied according to the capillary number.

For low Ca, e.g. $Ca = 0.1$, the deformation of the capsule is small, thereby preserving the membrane's undamaged state. Consequently, the maximum damage variable on the surface d_{max} remains at zero, and the squirmer swims along the membrane surface (cf. figure 3*a*,*b*).

With an augmented capillary number, $Ca = 0.11$, deformation of the capsule increases, and the strain energy reaches the threshold for the onset of brittle damage. The damage variable d_{max} then gradually increases but reaches a stable state, while the squirmer creates a ring-like damage area on the membrane surface (cf. figure 3*c*). And this state is defined as the damaged state.

With an even larger capillary number, $Ca = 0.12$, the membrane damage no longer remains in the stable regime, but increases, eventually leading to membrane rupture forming a scratch-like rupture area diagonally ahead of its swimming direction (cf. figure 3*d*). Accordingly, the damage variable d_{max} increases quickly and reaches its maximum in a short time, as shown in figure 3(*a*).

3.3. *Membrane rupture in different swimming modes*

The squirmer with different β is placed inside the capsule, and it is found find that the critical capillary number for membrane rupture depends on β.

In the case of a pusher-type squirmer ($\beta = -3$), the critical capillary number for membrane rupture, Ca_0, is in the range $0.11 < Ca_0 < 0.12$ when the initial incidence angle is $\theta = 30°$. As previously outlined, the pusher-type squirmer swims along the membrane, and membrane rupture occurs near the oblique front of the swimming direction (cf. figures 3(*d*) and 4(*a*), and supplementary movie 1).

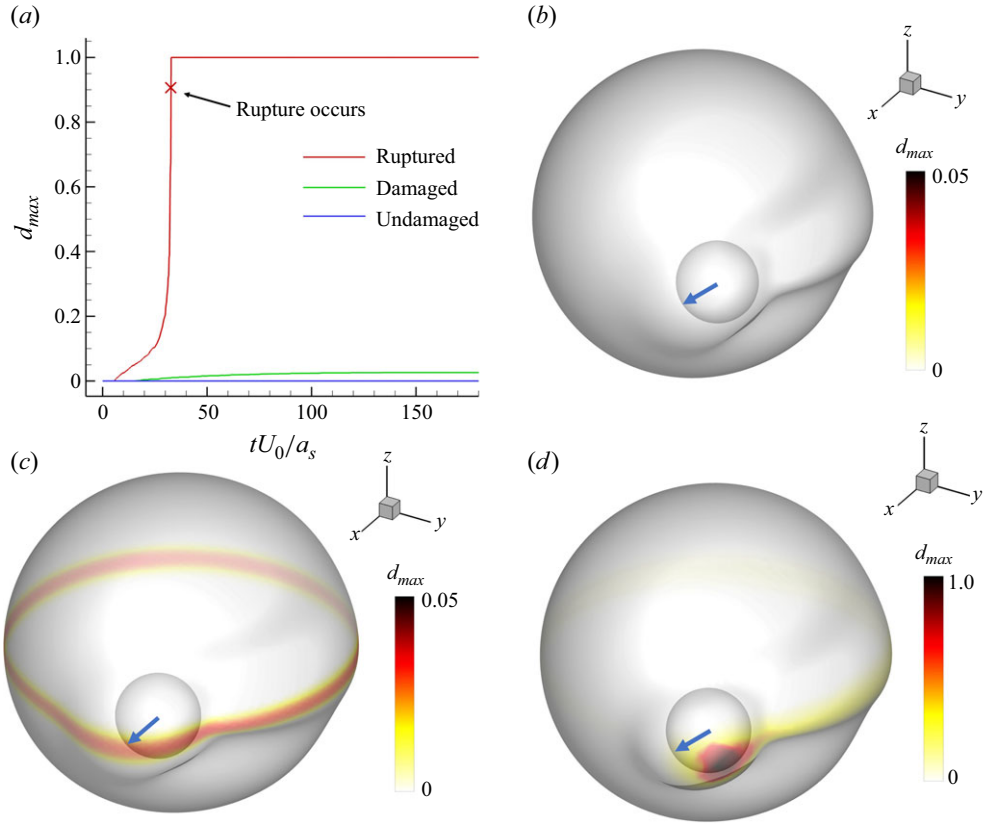

Figure 3. Different states of the capsule confining a pusher-type squirmer ($\beta = -3$): ruptured state ($Ca = 0.12$), damaged state ($Ca = 0.11$) and undamaged state ($Ca = 0.1$). (*a*) Damage evolution of the capsule with different Ca. When $Ca = 0.12$, the capsule is ruptured at $tU_0/a_s = 32.5$, whereas the damage to the membrane remains small below $Ca \leqslant 0.11$. Snapshots of (*b*) an undamaged state ($Ca = 0.1,\ tU_0/a_s = 50$), (*c*) a damaged state ($Ca = 0.11,\ tU_0/a_s = 150$), and (*d*) a ruptured state ($Ca = 0.12,\ tU_0/a_s = 32.5$). The initial incidence angle is set to $\theta = 30°$, and the colour band indicates the damage variable on the membrane.

In the case of a puller-type squirmer ($\beta = 3$) and a neutral-type squirmer ($\beta = 0$), the damage area is similar in appearance, forming a small damage patch in front of the squirmer, and breaking the membrane from the centre of the patch (see figure 4(*b*,*c*) and supplementary movies 2 and 3). The time to membrane rupture for the puller-type and neutral-type squirmers is $tU_0/a_s \approx 10$, which is faster than for the pusher-type squirmer ($tU_0/a_s = 32.5$). Despite the similarity in the motions of the squirmer and the formations of membrane damage for the puller-type and neutral-type squirmers, their critical capillary numbers Ca_0 are different, estimated to be $0.12 < Ca_0 < 0.13$ for a puller-type squirmer, and $0.1 < Ca_0 < 0.11$ for a neutral-type squirmer.

Here, we compare the present results with the study by Grandmaison *et al.* (2021), who investigated capsule rupture in simple shear flow.

Previous studies have defined the capillary number as $Ca_{pre} = \mu\gamma a_c/G_s$, where γ corresponds to the shear rate. However, due to the difference in capsule radius ($a_c/a_c^{pre} = 4$), it is necessary to divide Ca_{pre} by 4, converting to the one based on the capsule radius for a meaningful comparison with our Ca_0. When they used $Y_D/G_s = 0.2$ and $Y_C/G_s = 2.0$, the capsule is damaged with $Ca_{pre}/4 \approx 0.1$, and broken with $Ca_{pre}/4 \approx 0.18$. On the other hand, when we choose the same Y_D and Y_C in the present setting, the capsule can be

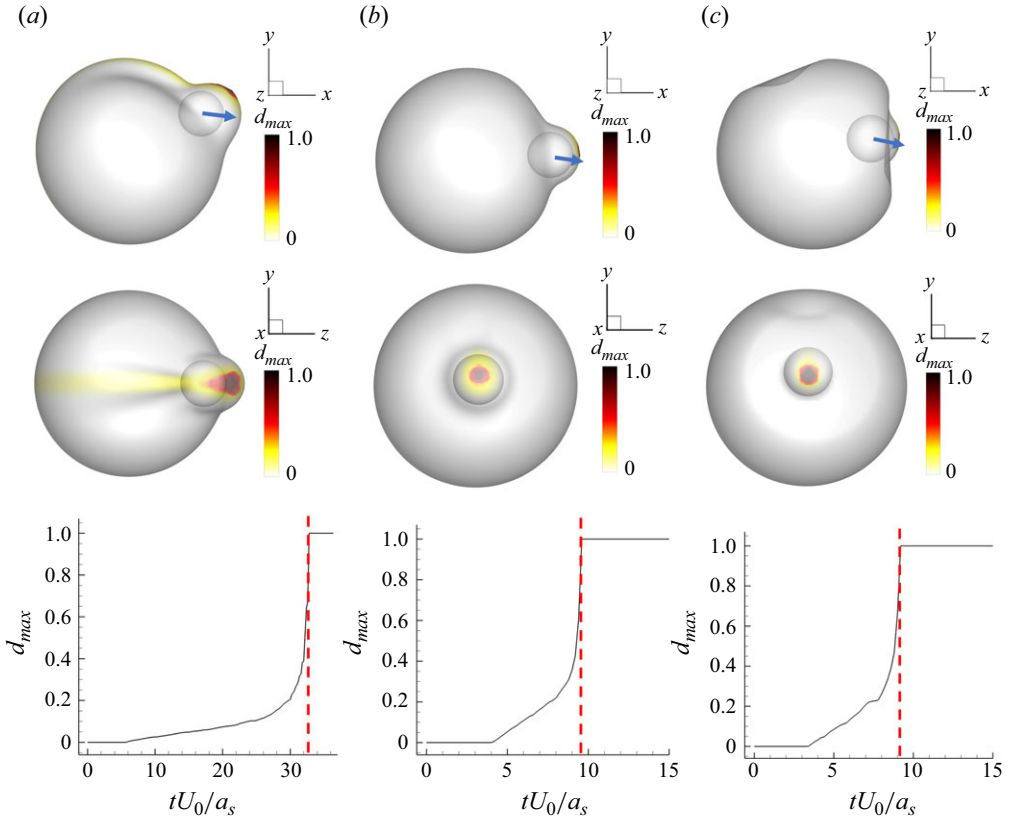

Figure 4. Rupture of the capsule by squirmers with different swimming modes: (*a*) a pusher-type squirmer ($\beta = -3$), (*b*) a neutral-type squirmer ($\beta = 0$), and (*c*) a puller-type squirmer ($\beta = 3$). The time of the rupture is indicated by the broken line in the graph; $tU_0/a_s = 32.5$ with a pusher-type squirmer, $tU_0/a_s = 9.6$ with a neutral-type squirmer, and $tU_0/a_s = 9.1$ with a puller-type squirmer. The upper panels are viewed from the (x, y)-plane, while the middle panels are viewed from the (y, z)-plane. The initial incidence angle is set to $\theta = 30°$.

damaged with $Ca_0 \approx 0.1$, and broken with $Ca_0 \approx 0.13$. These results indicate that capsules can be broken more easily when subjected to the action of an internal swimmer than when subjected to a simple shear flow.

3.4. *Phase diagram of membrane damage*

The effect of capillary number Ca and swimming mode β on the membrane damage is summarised in figure 5. The initial angle of incidence is set to $\theta = 30°$ for all cases, and the effect of θ is explained in the next subsection.

When Ca is less than 0.05, the membrane deformation is sufficiently small that the strain energy does not reach the threshold for onset of brittle damage for all β. In regimes where Ca is greater than 0.05, the damage state depends on the swimming mode β. In the case of a strong pusher-type squirmer, i.e. in the $\beta < -2$ regime, the squirmer tends to swim along with the membrane surface, and the undamaged regime expands with $|\beta|$. In this regime, the critical capillary number for membrane rupture Ca_0 is close to the Ca value at which brittle damage begins, and the undamaged and rupture states are close together. However, in the case of a weak pusher-type squirmer ($-2 \leqslant \beta < -1$), the squirmer tends to swim towards the membrane surface, and the membrane is susceptible

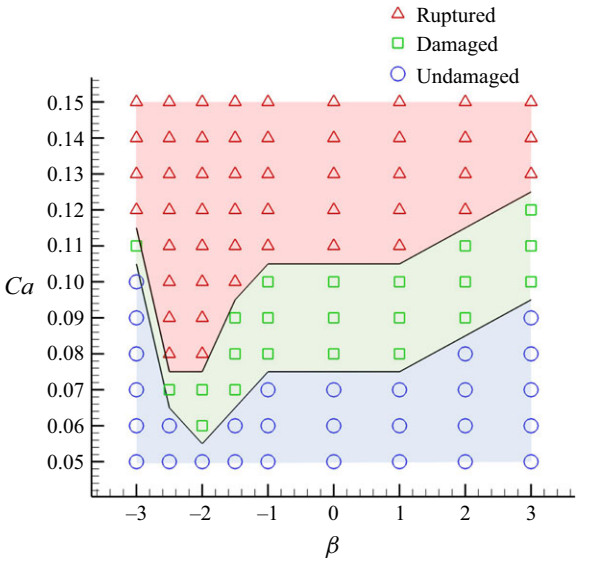

Figure 5. Phase diagram of damage development in β and Ca space. The initial incidence angle is set to $\theta = 30°$.

to damage from the recirculating flow in front of the squirmer (cf. figure 1*b*), with Ca_0 reaching a minimum value at $\beta = -2$, where the swimming direction undergoes a transition from being aligned with the surface to being oriented against it. In regimes where $\beta \geqslant -1$, in particular where $\beta \geqslant 1$, the undamaged regime tends to widen as β increases. In the $-1 < \beta < 1$ regime, the flow generated by the squirmer is relatively smooth and weak, and all squirmers in this regime tend to swim towards the membrane surface, thus the critical capillary numbers become the same. Conversely, in the $\beta > 1$ regime, the flow in front of the squirmer tends to draw the capsule membrane close to the squirmer, thereby cancelling out a part of the deformation towards outside, and thus expanding the undamaged region as β increases.

3.5. *Effect of incidence angle*

In the following investigation, the influence of the incidence angle θ is examined by varying the initial position of the squirmer y (see figure 1*a*). The swimming mode β is set to $\beta = -3$, 0, 3, and the results are shown in figure 6.

When $\beta = -3$, the critical capillary number increases with the incidence angle (see figure 6*a*), indicating that the capsule becomes harder to damage. When the angle of incidence is large, the initial swimming direction of the squirmer is almost tangential to the capsule surface, and it swims stably along the surface (see supplementary movie 5). Conversely, when the angle of incidence is small, the initial swimming direction is almost perpendicular to the capsule surface, resulting in severe deformation of the capsule (see supplementary movie 4). This makes the capsule more susceptible to damage.

When $\beta = 0$ and 3, the critical capillary number is found to be unaffected by the incidence angle (figure 1*b*,*c*), indicating that the occurrence of brittle damage is independent of the initial condition. In the case of a puller-type squirmer or a neutral-type squirmer, the squirmer tends to swim perpendicular to the capsule surface. Therefore, in the present study, the direction of swimming near the membrane is determined regardless of the initial conditions, and as a result, θ dependence cannot be observed (see supplementary movies 6 and 7).

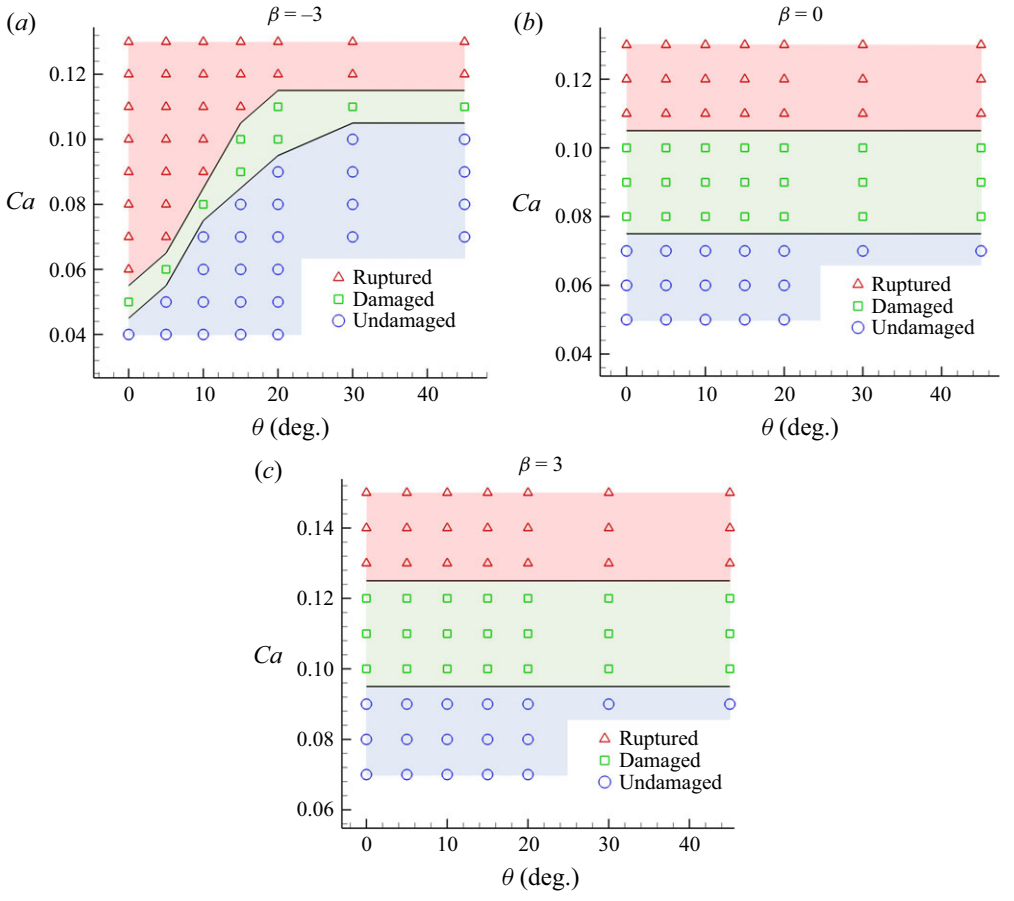

Figure 6. Effect of the initial incidence angle θ: capsule enclosing (a) a pusher-type squirmer ($\beta = -3$), (b) a neutral-type squirmer ($\beta = 0$), and (c) a puller-type squirmer ($\beta = 3$).

4. Rupture control by external magnetic torque

Then comes the question, can we manipulate the damage of a capsule? Here, we consider using an external magnetic field to manipulate damage by controlling the swimming direction of the squirmer. We assume that the artificial squirmer is composed of a magnetic material with uniform magnetisation $\boldsymbol{M}$, and the density of the magnetic field is considered as $\boldsymbol{B}$. The magnetic torque exerted on the squirmer is then defined in the equation (Abbott, Diller & Petruska 2020)

$$\boldsymbol{T}_m = V_s \boldsymbol{M} \times \boldsymbol{B}, \tag{4.1}$$

where V_s corresponds to the volume of the squirmer. We also assume that the orientation vector $\boldsymbol{e}$ of the squirmer is the same as the magnetisation, and the magnetic field $\boldsymbol{B}$ is in the same plane as the swimming direction. Thus the magnetic torque exerted on the squirmer can be written as

$$\left.\begin{aligned} \boldsymbol{T}_m &= A_m \boldsymbol{e} \times \boldsymbol{b}, \\ \boldsymbol{b} &= \boldsymbol{B}/|\boldsymbol{B}|, \end{aligned}\right\} \tag{4.2}$$

where A_m is the amplitude of the magnetic torque, and $\boldsymbol{b}$ is the unit vector of the magnetic field $\boldsymbol{B}$.

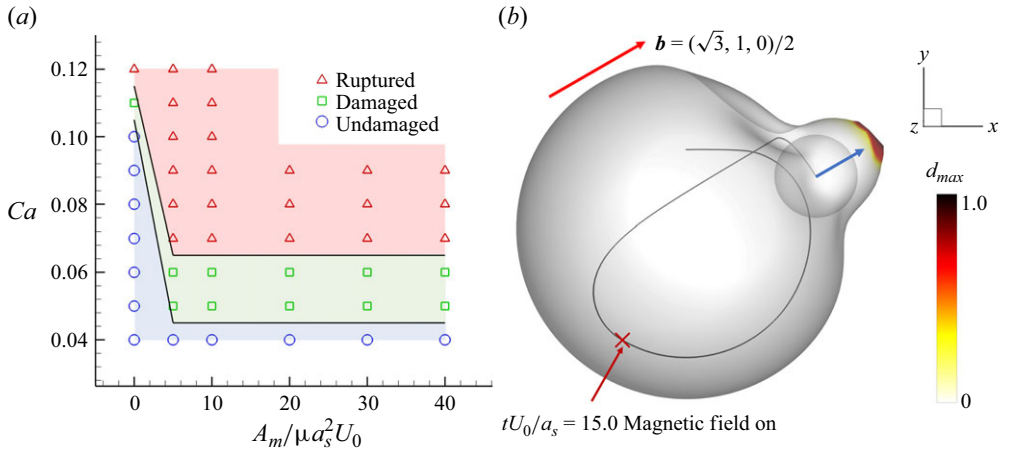

Figure 7. Rupture of the capsule with a pusher-type squirmer inside controlled ($\beta = -3$) by a constant external magnetic torque. The normalised magnetic field vector is set to $\boldsymbol{b} = (\sqrt{3}, 1, 0)/2$, and the initial incidence angle is set to $\theta = 30°$. (*a*) Effect of the amplitude of external magnetic torque A_m. (*b*) Behaviour of the pusher-type squirmer until the membrane becomes ruptured. Magnetic torque is applied at $tU_0/a_s = 15$ (indicated by the cross) to control the swimming direction of the squirmer. By applying the magnetic torque with amplitude $A_m/\mu a_s^2 U_0 = 30$, the stable circular swimming of the inside squirmer changes to a one-directional swimming, which allows the squirmer to break the capsule (Ca is set to 0.07).

4.1. *Breaking a harder capsule with a static magnetic field*

First, drug release is assumed, then an external magnetic field is applied to rupture the elastically deforming capsule membrane. A pusher-type squirmer ($\beta = -3$) is used, and a static magnetic field is considered for the external magnetic field, $\boldsymbol{b} = (\sqrt{3}, 1, 0)/2$.

The capillary number is set to $Ca = 0.07$ to correspond to a brittle damage-free regime with stable elastic deformation except for initial defects with initial incidence angle less than 10°.

The magnetic torque activates at the dimensionless time $tU_0/a_s = 15.0$, and its amplitude is set to $A_m/\mu a_s^2 U_0 = 30$. Before the activation of the magnetic torque, the squirmer swims along with the surface. However, after the activation of the magnetic field, the squirmer's movement is directed towards the direction of the magnetic field $\boldsymbol{b}$ due to the magnetic torque, as shown in figure 7 and supplementary movie 8. The second incident angle is smaller, and is accompanied by deformation of the rupture regime. This results in the eventual rupture of the membrane.

We then investigate the effect of A_m on the critical capillary number. As demonstrated in figure 7(*a*), the critical capillary number undergoes a substantial decrease due to the influence of the external magnetic torque A_m. The findings suggest that the rupture of the membrane can be controlled by the squirmer through the application of a sufficiently large external torque.

4.2. *Preserving a capsule by a rotational magnetic field*

Next, the potential of a rotating magnetic field in preventing the rupture of a softer capsule is explored. A pusher-type squirmer ($\beta = -3$) is employed as the internal swimmer. Under these conditions, the capsule remains in the ruptured regime in the absence of magnetic torque. The rotating magnetic field is defined as $\boldsymbol{b} = (\cos \omega_m t, -\sin \omega_m t, 0)$, where t is time. The magnitude of the torque is set to $A_m/\mu a_s^2 U_0 = 40$, and the angular velocity ω_m is parametrised (see figure 8).

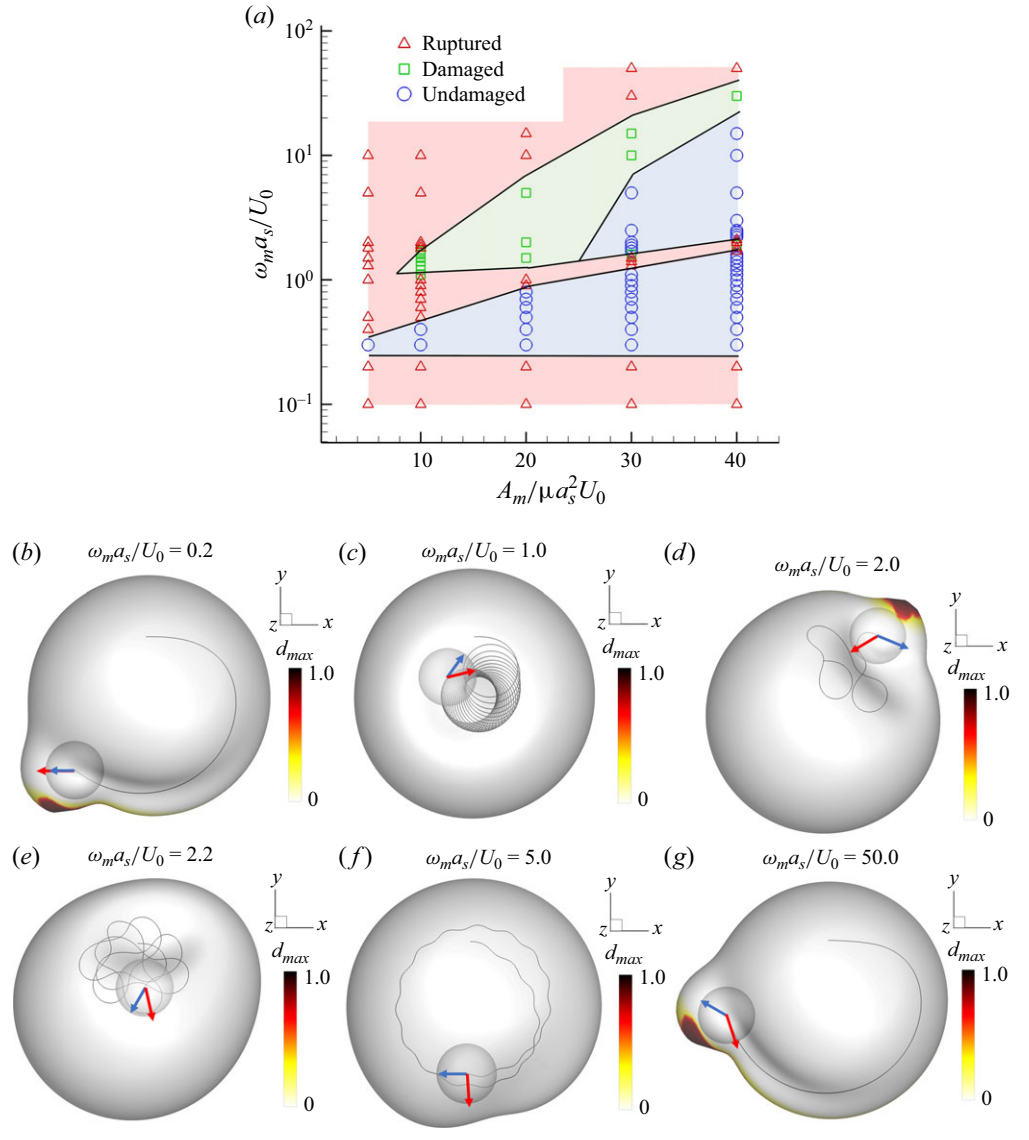

Figure 8. Rupture of the capsule with a pusher-type squirmer inside controlled by a rotating magnetic field; $\beta = -3$, $Ca = 0.15$ and $\theta = 30°$ for all cases. (*a*) Phase diagram in A_m and ω_m space. (*b–g*) Effects of the angular velocity on the swimming of the squirmer: $\omega_m a_s/U_0 = 0.2$, 1.0, 2.0, 2.2, 5.0, 50.0, respectively, while the amplitude is set to $A_m/\mu a_s^2 U_0 = 40$ for all cases. The black line indicates the swimming trajectory of the squirmer, and the blue and the red arrows correspond to the swimming direction $\boldsymbol{e}$ and the normalised magnetic field vector $\boldsymbol{b}$, respectively.

When the angular velocity is sufficiently small, e.g. $\omega_m a_s/U_0 = 0.2$ in figure 8(*b*), the magnetic field changes too slowly to make the swimmer move away from the membrane. This condition is analogous to the absence of a magnetic field, and the capsule reaches a rupture state (see supplementary movie 9). When the angular velocity of the magnetic field is comparable to the swimming speed ($0.2 < \omega_m a_s/U_0 \leqslant 1.5$), the squirmer traces a circular orbit of its radius, and the interaction with the membrane also becomes weak. Therefore, the capsule membrane is preserved (cf. figure 8(*c*) and supplementary

movie 10). However, when the angular velocity is approximately $1.5 < \omega_m a_s / U_0 \leqslant 2$, the swimming path becomes unstable, and the increased frequency of near-field interactions between the capsule and the squirmer tends to increase the susceptibility to rupture (cf. figure 8(*d*) and supplementary movie 11). Then in the regime with larger ω_m ($2 < \omega_m a_s / U_0 \leqslant 10$), the angular velocity of the magnetic field gradually becomes dominant in relation to the angular velocity of swimming ($\omega_m > |\boldsymbol{\Omega}|$), and the swimming trajectory again approaches a smooth circular path (cf. figure 8(*e*,*f*) and supplementary movies 12 and 13). However, with extremely large angular velocities, e.g. $\omega_m a_s / U_0 = 50$ in figure 8(*g*), the magnetic field undergoes such rapid changes that the swimmer is unable to maintain its course. Consequently, the motion of the squirmer reverts to a state of sufficiently small angular velocity, resulting in the membrane reaching a rupture state (see supplementary movie 14).

The phase diagram of the membrane damage due to torque magnitude A_m and angular velocity ω_s is summarised in figure 8(*a*). Evidence suggests that there is indeed a damage-free region, indicating the potential for utilising the rotating magnetic field as a soft capsule transport technique.

5. Conclusion

In this study, we proposed a capsule enclosing a microswimmer, and focused on the damage behaviour of the capsule membrane. In the present simulation, three distinct capsule states were obtained: namely, the undamaged state, the damaged state, and the rupture state.

It is important to note that the repulsive force determines the minimum distance between the squirmer and the capsule membrane, thus it has the capacity to affect the result quantitatively. In this study, the minimum repulsive force required for a mesh-size separation between the squirmer and the capsule membrane was determined. However, for repulsive forces below this level, the calculations become unstable due to a lack of resolution in expressing the lubrication flow.

In the context of the fixed swimming mode, an increase in Ca has been observed to result in capsules undergoing greater deformation, attributable to hydrodynamic interaction. A comparison of these findings with those of a previous study (Grandmaison *et al.* 2021) reveals a parallel in the damage development process of the capsules. Specifically, the damage variable exhibits a steady increase below $d \approx 0.2$, and subsequently experiences a steep rise until reaching $d = 1$. Meanwhile, we find that our capsule can be damaged more easily (with a smaller Ca_0). The underlying cause of these discrepancies can be attributed to the hydrodynamic interaction. Grandmaison *et al.* (2021) made their capsule deformed by simple shear flow, a moderate interaction affecting the whole capsule, while we use an inside microswimmer, generating a strong interaction near the microswimmer. Also, comparing our results with Leopércio *et al.* (2021), we find the same trend of damage: a capsule with a larger capillary number Ca and larger deformation can be damaged more easily.

When Ca is held constant, the difference in the swimming mode β can be categorised into two distinct behaviours of the inside squirmer: sliding along the capsule surface ($\beta < -2$), and swimming towards the capsule surface ($\beta \geqslant -2$). According to previous research (Ishikawa 2019), a pusher-type squirmer ($\beta < 0$) tends to turn away from the free surface, while a neutral-type squirmer ($\beta = 0$) or a puller-type squirmer ($\beta > 0$) tends to swim towards the free surface. In our results, a strong pusher-type squirmer ($\beta < -2$), a neutral-type squirmer ($\beta = 0$) and a puller-type squirmer ($\beta > 0$) have the same motion with Ishikawa (2019), while a weak pusher-type squirmer ($-2 \leqslant \beta < 0$) also

swims towards the capsule surface. The reason for this phenomenon is attributed to the soft capsule surface. When a weak pusher-type squirmer first encounters the capsule surface, the torque received is not strong enough to make it completely turn away from the capsule surface, and it is then surrounded by the capsule membrane because of deformation. Also, in the results of Ishikawa (2019), a pusher-type squirmer receives larger rotational torque when swimming parallel to the free surface than when swimming towards the surface. In our results, therefore, a weak pusher-type squirmer receives larger torque from its side than from its front, and becomes no longer able to turn away from the capsule surface. In terms of damage of the capsule, in the situation $\beta < -2$, a squirmer with smaller β receives a larger rotational torque to make itself turn away from the capsule surface. This results in a weaker hydrodynamic interaction with the capsule, and an increased threshold Ca. But in the situation $\beta \geqslant -2$, all kinds of squirmers swim towards the capsule surface. As β increases, the deformation at the capsule surface is gradually annulled by the hydrodynamic interaction, and the threshold Ca also increases. In terms of damage manipulation, it has been found that the application of a static magnetic torque to the microswimmer results in the rupture state being attained at a lower $Ca = 0.07$ as compared to the value $Ca = 0.12$ observed in the absence of a static torque. Conversely, when a rotational magnetic torque is applied to the microswimmer, it is observed that the capsule can be maintained in an undamaged state at a high capillary number ($Ca = 0.15$) if the appropriate rotational magnetic field is applied (cf. figure 8).

When considering a real microswimmer, a Janus particle constitutes a viable candidate. A Janus particle is composed of two distinct materials, and can be propelled by a concentration difference, electrical or thermal conductivity of the surrounding fluid. For instance, a metal rod made of platinum and gold can be propelled by its self-electrophoresis (Moran & Posner 2017). When such a metal rod is immersed in hydrogen peroxide, peroxide oxidation occurs at the platinum end, and peroxide reduction occurs at the gold end. The oxidation reaction produces protons, while the reduction reaction consumes them, thereby establishing a proton concentration gradient via the electrochemical reactions occurring on the nanomotor surface. The ions drag fluid in the same direction, leading to relative motion between the particle and the fluid such that the motor moves with the platinum end directed forwards. In the mathematical analysis of phoretic microswimmers, the fluid domain is commonly divided into two regions: the bulk region, and the interfacial region surrounding the particle (Moran & Posner 2017). Assuming that phoretic effects are confined to the thin interfacial region, such effects can be represented as surface slip velocities. Therefore, a phoretic microswimmer can be modelled as a squirmer. Control of such microswimmers can be achieved through magnetism by substituting one metal with a magnetic metal, such as Janus particles of a gold–nickel alloy, as demonstrated in the study by Wang *et al.* (2006).

In the context of the capsule, previous research focused on the vesicle membrane, as evidenced by the work of Nagard *et al.* (2022), who put several inside giant unilamellar vesicles. The vesicle membrane deformed enormously due to bacterial movement, yet it remained intact, suggesting that the lipid molecules that make up the vesicle membrane may flow in response to deformation, thereby preventing rupture. However, the fluidity of vesicle membranes poses challenges in terms of control over membrane breakdown. In contrast, a capsule does not fluidise because it has an elastic membrane, and brittle fracture occurs when local deformation exceeds a threshold value. We therefore focus on the control of substance release by an elastic capsule membrane rather than by a vesicle membrane.

In a previous study, for instance, a capsule was fabricated using polysiloxane, which possesses elastic modulus approximately $G_s \sim 5 \times 10^{-5}$ N m^{-1} (Feinberg, Funderburgh

& Simko 2015). Another example can be a capsule made by a ghost cell of a red blood cell membrane, whose elastic modulus is $G_s \sim 10^{-6}$ N m^{-1}, as cited in Omori *et al.* (2012). Examples of squirmers include Janus particles and swimming microorganisms. Recent studies have revealed that gold–platinum type Janus particles exhibit swimming velocity 25 μm s^{-1} (Moran & Posner 2017), while bacteria *E. coli* have been documented to swim at velocity 1 μm s^{-1} (Ishikawa 2024*b*). Additionally, microalgae *Volvox* have been recorded to swim at velocity 250 μm s^{-1} (Drescher *et al.* 2009), and ciliate *Paramecium* have been recorded to swim at velocity 1 mm s^{-1} (Ishikawa 2024*b*). Assuming the surrounding fluid to be oleic acid, whose viscosity is approximately $\mu \sim 5 \times 10^{-2}$ Pa s (Sagdeev *et al.* 2019), the critical speed that can break the polysiloxane capsule is $U \sim 100$ μm s^{-1}. However, if the capsule is composed of a ghost cell derived from a red blood cell membrane, then the critical speed required for capsule rupture decreases to approximately $U \sim 2$ μm s^{-1}. It is then considered that both Janus swimmers and microorganisms can disrupt these capsules from the inside.

The findings of this study demonstrate that the impairment of the capsule membrane can be regulated by modifying its capillary number, as well as the swimming mode and incidence angle of the inside microswimmer. Furthermore, the implementation of a magnetic field enables the modulation of the internal microswimmer's trajectory, thereby affecting the integrity of the capsule membrane. It is imperative to comprehend the interplay between the damage to the capsule membrane and the motion of the internal microswimmer, as evidenced by these findings. Furthermore, they establish the basis for potential applications, including controlled drug release.

Supplementary movies. Supplementary movies are available at https://doi.org/10.1017/jfm.2025.10238.

Acknowledgements. This work was supported by JST SPRING (grant no. JPMJSP2114), JST PRESTO (grant no. J210002385) and JSPS KAKENHI (grant nos 24H01458, 21H04999 and 21H05308).

Declaration of interests. The authors report no conflict of interest.

References

Abbott, J.J., Diller, E. & Petruska, A.J. 2020 Magnetic methods in robotics. *Annu. Rev. Control Robot. Auton. Syst.* **3** (1), 57–90.

Barthès-Biesel, D. 1980 Motion of a spherical microcapsule freely suspended in a linear shear flow. *J. Fluid Mech.* **100** (4), 831–853.

Barthès-Biesel, D., Diaz, A. & Dhenin, E. 2002 Effect of constitutive laws for two-dimensional membranes on flow-induced capsule deformation. *J. Fluid Mech.* **100**, 211–222.

Besson, J., Cailletaud, G., Chaboche, J.L. & Forest, S. 2010 *Non-Linear Mechanics of Materials*. Springer.

Bhujbal, S.V., de Vos, P. & Niclou, S.P. 2014 Drug and cell encapsulation: alternative delivery options for the treatment of malignant brain tumors. *Adv. Drug Deliv. Rev.* **67–68**, 142–153.

Blake, J.R. 1971 A spherical envelope approach to ciliary propulsion. *J. Fluid Mech.* **46** (1), 199–208.

Brady, J.F. & Bossis, G. 1985 The rheology of concentrated suspensions of spheres in simple shear flow by numerical simulation. *J. Fluid Mech.* **155**, 105–129.

Chang, K.S. & Olbricht, W.L. 1993 Experimental studies of the deformation and breakup of a synthetic capsule in steady and unsteady simple shear flow. *J. Fluid Mech.* **250**, 609–633.

Daddi-Moussa-Ider, A., Goh, S., Liebchen, B., Hoell, C., Mathijssen, A.J.T.M., Guzmán-Lastra, F., Scholz, C., Menzel, A.M. & Löwen, H. 2019 Membrane penetration and trapping of an active particle. *J. Chem. Phys.* **150** (6), 064906.

Dias, M.A. & Powers, T.R. 2013 Swimming near deformable membranes at low Reynolds number. *Phys. Fluids.* **25** (10), 101901.

Drescher, K., Leptos, K.C., Tuval, I., Ishikawa, T., Pedley, T.J. & Goldstein, R.E. 2009 Dancing *Volvox*: hydrodynamic bound states of swimming algae. *Phys. Rev. Lett.* **102** (16), 168101.

DUPONT, C., TALLEC, P.LE, BARTHÈS-BIESEL, D., VIDRASCU, M. & SALSAC, A.-V. 2015 Dynamics of a spherical capsule in a planar hyperbolic flow: influence of bending resistance. *Proc. IUTAM* **16**, 70–79.

FEINBERG, A.W., FUNDERBURGH, J.L. & SIMKO, R. 2015 Polysiloxane substrates with highly-tunable elastic modulus. United States Patent Application Publication US2015/0010919A1.

FESSLER, F., WITTMANN, M., SIMMCHEN, J. & STOCCO, A. 2024 Autonomous engulfment of active colloids by giant lipid vesicles. *Soft Matt.* **20** (30), 5904–5914.

FOESSEL, É., WALTER, J., SALSAC, A.-V. & BARTHÈS-BIESEL, D. 2011 Influence of internal viscosity on the large deformation and buckling of a spherical capsule in a simple shear flow. *J. Fluid Mech.* **672**, 477–486.

FRIEDMAN, S.P. & MUALEM, Y. 1994 Diffusion of fertilizers from controlled-release sources uniformly distributed in soil. *Fertil. Res.* **39** (1), 19–30.

GRANDMAISON, N., BRANCHERIE, D. & SALSAC, A.V. 2021 Modelling of damage of a liquid-core microcapsule in simple shear flow until rupture. *J. Fluid Mech.* **914**, A25.

HELFRICH, W. 1973 A spherical envelope approach to ciliary propulsion. *Z. Naturforsch. C* **28** (11–12), 693–703.

HUANG, H.W., SAKAR, M.S., PETRUSKA, A.J., PANÉ, S. & NELSON, B.J. 2016 Soft micromachines with programmable motility and morphology. *Nat. Commun.* **7** (1), 12263.

HUANG, Z., OMORI, T. & ISHIKAWA, T. 2020 Active droplet driven by a collective motion of enclosed microswimmers. *Phys. Rev. E* **102** (2), 022603.

HUSMANN, M., REHAGE, H., DHENIN, E. & BARTHÈS-BIESEL, D. 2005 Deformation and bursting of nonspherical polysiloxane microcapsules in a spinning-drop apparatus. *J. Colloid. Interface Sci.* **282** (1), 109–119.

ISHIKAWA, T. 2019 Swimming of ciliates under geometric constraints. *J. Appl. Phys.* **125** (20), 200901.

ISHIKAWA, T. 2024*a* Fluid dynamics of squirmers and ciliated microorganisms. *Annu. Rev. Fluid Mech.* **56** (1), 119–145.

ISHIKAWA, T. 2024*b* Fluid dynamics of squirmers and ciliated microorganisms. *Annu. Rev. Fluid Mech.* **56** (1), 119–145.

ISHIKAWA, T., SIMMONDS, M.P. & PEDLEY, T.J. 2006 Hydrodynamic interaction of two swimming model micro-organisms. *J. Fluid Mech.* **568**, 119–160.

JAMBON-PUILLET, E., JONES, T.J. & BRUN, P.T. 2020 Deformation and bursting of elastic capsules impacting a rigid wall. *Nat. Phys.* **16** (5), 585–589.

KAMAT, A., PALIN, D., LUBELLI, B. & SCHLANGEN, E. 2024 Capsule controlled release of crystallisation inhibitors in mortars. *Mater. Des.* **244**, 113156.

KAWAKAMI, S. & VLAHOVSKA, P.M. 2025 Migration and deformation of a droplet enclosing an active particle. *J. Fluid Mech.* **1007**, A41.

KOLEVA, I. & REHAGE, H. 2012 Deformation and orientation dynamics of polysiloxane microcapsules in linear shear flow. *Soft Matt.* **13** (13), 3681–3693.

KREE, R., RÜCKERT, L. & ZIPPELIUS, A. 2021 Dynamics of a droplet driven by an internal active device. *Phys. Rev. Fluids* **6** (3), 034201.

LAC, E., BARTHÈS-BIESEL, D., PELEKASIS, N.A. & TSAMOPOULOS, J. 2004 Spherical capsules in three-dimensional unbounded Stokes flows: effect of the membrane constitutive law and onset of buckling. *J. Fluid Mech.* **516**, 303–334.

LEOPÉRCIO, B.C., MICHELON, M. & CARVALHO, M.S. 2021 Deformation and rupture of microcapsules flowing through constricted capillary. *Sci. Rep.* **11** (1), 7707.

LIGHTHILL, M.J. 1952 On the squirming motion of nearly spherical deformable bodies through liquids at very small Reynolds numbers. *Commun. Pure Appl. Maths* **5** (2), 109–118.

LOZANO, C., HAGEN, B.T., LÖWEN, H. & BECHINGER, C. 2016 Phototaxis of synthetic microswimmers in optical landscapes. *Nat. Commun.* **7** (1), 12828.

MARIGO, J.J. 1985 Modelling of brittle and fatigue damage for elastic material by growth of microvoids. *Engng Fract. Mech.* **21** (4), 861–874.

MATSUNAGA, D., IMAI, Y., YAMAGUCHI, T. & ISHIKAWA, T. 2015 Deformation of a spherical capsule under oscillating shear flow. *J. Fluid Mech.* **762**, 288–301.

MATSUNAGA, D., IMAI, Y., YAMAGUCHI, T. & ISHIKAWA, T. 2016 Rheology of a dense suspension of spherical capsules under simple shear flow. *J. Fluid Mech.* **786**, 110–127.

MORAN, J.L. & POSNER, J.D. 2017 Phoretic self-propulsion. *Annu. Rev. Fluid Mech.* **49** (1), 511–540.

LE NAGARD, L., BROWN, A.T., DAWSON, A., MARTINEZ, V.A., POON, W.C.K. & STAYKOVA, M. 2022 Encapsulated bacteria deform lipid vesicles into flagellated swimmers. *Proc. Natl Acad. Sci. USA* **119** (34), e2206096119.

OMORI, T., IMAI, Y., YAMAGUCHI, T. & ISHIKAWA, T. 2012 Reorientation of a nonspherical capsule in creeping shear flow. *Phys. Rev. Lett.* **108** (13), 138102.

OU-YANG, Z. & HELFRICH, W. 1989 Bending energy of vesicle membranes: general expressions for the first, second, and third variation of the shape energy and applications to spheres and cylinders. *Phys. Rev. A* **39** (10), 5280–5288.

POZRIKIDIS, C. 2010 *Computational Hydrodynamics of Capsules and Biological Cells*. CRC Press.

REIGH, S.Y., ZHU, L., GALLAIRE, F. & LAUGA, E. 2017 Swimming with a cage: low-Reynolds-number locomotion inside a droplet. *Soft Matt.* **13** (17), 3161–3173.

SAGDEEV, D., GABITOV, I., ISYANOV, C., KHAIRUTDINOV, V., FARAKHOV, M., ZARIPOV, Z. & ABDULAGATOV, I. 2019 Densities and viscosities of oleic acid at atmospheric pressure. *J. Am. Oil Chem. Soc.* **96** (6), 647–662.

SHI, X. & TAN, T. 2002 Preparation of chitosan/ethylcellulose complex microcapsule and its application in controlled release of vitamin d_2. *Biomaterials* **23**, 4469–4473.

SKIRTACH, A.G., KARAGEORGIEV, P., BÉDARD, M.F., SUKHORUKOV, G.B. & MÖHWALD, H. 2008 Reversibly permeable nanomembranes of polymeric microcapsules. *J. Am. Chem. Soc.* **130** (35), 11572–11573.

TAKATORI, S.C. & SAHU, A. 2020 Active contact forces drive nonequilibrium fluctuations in membrane vesicles. *Phys. Rev. Lett.* **124** (15), 158102.

VUTUKURI, H.R., HOORE, M., ABAURREA-VELASCO, C., VAN BUREN, L., DUTTO, A., AUTH, T., FEDOSOV, D.A., GOMPPER, G. & VERMANT, J. 2020 Active particles induce large shape deformations in giant lipid vesicles. *Nature* **586** (7827), 52–69.

WALTER, A., REHAGE, H. & LEONHARD, H. 2001 Shear induced deformation of microcapsules: shape oscillations and membrane folding. *Colloid Surf. A: Physicochem. Engng Aspects* **183**, 123–132.

WALTER, J., SALSAC, A.V., BARTHÈS-BIESEL, D. & TALLEC, P.L. 2010 Coupling of finite element and boundary integral methods for a capsule in a Stokes flow. *Intl J. Numer. Meth. Engng* **83** (7), 829–850.

WANG, Y., HERNANDEZ, R.M. JR, BARTLETT, D.J., BINGHAM, J.M., KLINE, T.R., SEN, A. & MALLOUK, T.E. 2006 Bipolar electrochemical mechanism for the propulsion of catalytic nanomotors in hydrogen peroxide solutions. *Langmuir* **22** (25), 10451–10456.

WU, C., OMORI, T. & ISHIKAWA, T. 2024 Surface-active microrobots can propel through blood faster than inert microrobots. *PNAS Nexus* **3** (10), 463.